Mathematical and Computational Applications

MDPI

Article

Impact Loading on a Patient-Specific Head Model: The Significance of Brain Constitutive Models and Loading Location

Amirhossein Gandomirouzbahani [1,2], Hadi Taghizadeh [3,*], Iman Z. Oskui [4,*] and Fábio A. O. Fernandes [1,2,*]

[1] TEMA—Centre for Mechanical Technology and Automation, Department of Mechanical Engineering, University of Aveiro, Campus de Santiago, 3810-193 Aveiro, Portugal; amirhossein.gandomi@ua.pt
[2] LASI—Intelligent Systems Associate Laboratory, 4800-058 Guimarães, Portugal
[3] Tissue Mechanics Laboratory, Faculty of Biomedical Engineering, Sahand University of Technology, Tabriz 51335/1996, Iran
[4] Biomechanical Engineering Group, Faculty of Biomedical Engineering, Sahand University of Technology, Tabriz 51335/1996, Iran
* Correspondence: taghizadeh@sut.ac.ir (H.T.); zoljanahi@sut.ac.ir (I.Z.O.); fabiofernandes@ua.pt (F.A.O.F.); Tel.: +9841-33-458-415 (H.T.); +9841-33-458-412 (I.Z.O.)

Abstract: Head impacts are common incidents that may cause traumatic brain injury (TBI), which imposes significant economic and social burdens. This study developed a patient-specific head model to address the significance of the brain's constitutive model and loading location on head impact. Two hyperelastic (Model I and Model II) constitutive models and one hyper-viscoelastic (Model III) constitutive model for the brain tissue were developed. In Models II and III, white and gray matter heterogeneities were included. Respective volumetric and deviatoric responses were compared for a frontal head impact. Then, the load was applied to the head's frontal, lateral, and posterior regions to report location-wise outcomes. The findings indicated that Model I, which was based on almost quasi-static experiments, underestimated the deviatoric responses. Although the pressure contours were similar for Models II and III, the latter included viscous effects and provided more accurate deviatoric responses. Lateral loading indicated a significantly higher risk of TBI. Interestingly, the deviatoric responses and strain energy density of the brain did not decay with relaxation of the impact load. Hence, the incidence of TBI should be explored after load relaxation.

Keywords: traumatic brain injury; hyper-viscoelastic constitutive modeling; deviatoric and volumetric response; stress analysis; finite element analysis

check for updates

Academic Editor: Joakim Sundnes

Received: 19 November 2024
Revised: 19 February 2025
Accepted: 19 February 2025
Published: 21 February 2025

Citation: Gandomirouzbahani, A.; Taghizadeh, H.; Oskui, I.Z.; Fernandes, F.A.O. Impact Loading on a Patient-Specific Head Model: The Significance of Brain Constitutive Models and Loading Location. *Math. Comput. Appl.* **2025**, *30*, 21. https://doi.org/10.3390/mca30020021

Copyright: © 2025 by the authors. Licensee MDPI, Basel, Switzerland. This article is an open access article distributed under the terms and conditions of the Creative Commons Attribution (CC BY) license (https://creativecommons.org/licenses/by/4.0/).

1. Introduction

According to a report by the Centers for Disease Control and Prevention, 1.7 million cases of traumatic brain injuries (TBIs) occur annually in the United States, and TBI was associated with 30.5% of all injury-related deaths [1]. The most common causes of TBI are falling, collisions with obstacles or objects, and vehicle accidents [2]. Respective treatment and rehabilitation costs are among the factors that seriously increase TBI's economic burden [1].

Human head models are computational tools and representations of the head that provide the possibility of detailed mechanical investigations using simulations. Essential anatomical components for developing finite element head models include the skull, brain tissue, and cerebrospinal fluid region [3,4].

Computational models of head impact conditions, including those addressing the heterogeneities of brain components and the incidence of TBI have been studied and

explored [5,6]. The finite element method has great potential in addressing different scenarios of head impact loading. Accurate model outcomes depend on accurate geometries, reliable mechanical properties (MPs), and realistic loading and boundary conditions.

Brain tissue mechanics researchers have demonstrated the brain tissue's nonlinear and different tension/compression responses [7,8], apparent homogenous behavior in certain regions, such as the cerebral cortex [9], and incompressibility [10]. Brain tissue is composed of white and gray matter; the stiffer behavior of the former [11] is complemented by the significantly more compliant response of the latter [12]. Therefore, the risk of TBI in different brain regions varies [13]. Newer studies, in which more evolved models were used to integrate nonlinear and time-dependent features to show the significant regional and temporal variability in brain tissue mechanics across various loading modes, have supported these findings [14]. While testing on tissue samples has been utilized for extraction of nonlinear and time-dependent behaviors of the brain [11,12], further advancements have also demonstrated the utility of magnetic resonance elastography as a non-invasive way to quantify such properties [15,16].

While some studies have examined more basic non-human models [17,18], with the progress of computing systems, complex models of human head dynamics, with sophisticated geometrical features and nonlinear MPs, have been proposed. Adding facial features improves the accuracy of the models [19]. In addition, adopting more complex geometries can partially improve the accuracy of simulation outcomes [20,21]. Some studies have also focused on more specific conditions, such as the mechanical behavior of cranial implants under impact loading in a finite element head model [22]. Furthermore, the integration of finite element models with advanced methods, like machine learning, has also been studied for practical aspects like functional outcomes in TBI [23].

Allocating suitable MPs for the heterogeneous and soft brain tissue is the pivotal point of head impact studies [19]. Earlier studies assumed linear elastic behavior for the head model components, including the brain [24]. Zhou et al. [25] stated the importance of mechanical differences between the white and gray matter in the impact response of the head model, and such differences have been further looked into in more recent studies [26]. Some other studies scaled the stiffness of the gray matter by a constant factor to obtain the MPs of the white matter [27]. For TBI simulations, such assumptions are inadequate, and separate allocation of material parameters for the white and gray matter is necessary.

Considering the time-dependent and viscoelastic characteristics observed from the brain tissue [12,28], viscoelastic constitutive models have been favored for mechanical description of the brain tissue [20,21,29–32], but, as mentioned above, hyper-viscoelastic models more accurately reflect the MPs of brain tissue. While nonlinear and time-dependent properties were considered for the white and gray matter in further improved head models, in some studies, a single constitutive model was considered for the whole brain [5,31–34]. In some other studies, high rates of impact loadings were neglected in proposed constitutive models [22,33,35], since these models are based on quasi-static experiments of the brain tissue [10,36].

To apply impact loading to the models, the head encounters impact from objects directed at specific regions [5,20,25] or collides with obstacles at defined velocities and positions [20,37]. In the modeling environment, impact conditions are established by applying force amplitude directly to a region of the head model over a specific period as a distributed load [21,29]. Furthermore, collision data are reconstructed in the laboratory to inform subsequent simulations, incorporating factors like acceleration [33,38]. In the recreation of blast exposures, pressure shocks are employed in shock tube simulations [34].

The location and direction of the impact loading on the head play principal roles in determining the extent of brain tissue damage. Some comprehensive studies in the

literature have addressed these parameters [37–40]. However, simplified geometries [39,41] or undemanding elastic and viscoelastic properties for the brain [24,38,40,42] are drawbacks of these studies. Also, some head models have been created for a specific group, such as infants [37], as this limits the adoption of the reported outcomes for general TBI cases.

The current study proposes a new finite element head model to address some of the mentioned limitations in the literature on head impact biomechanics and TBI investigation. The aim was to evaluate the influence of mechanical properties of brain tissue and loading locations on the brain's mechanical responses during head impacts, focusing on critical factors of TBI risk investigation. In this study, coefficients for constitutive models of brain tissue were determined to ensure suitable performance in investigating impact loading conditions.

The geometry of the head was imported into the numerical modeling environment with reasonable accuracy. In the investigation process, three constitutive models were examined to select a refined model for the brain for impact simulations. The white and gray matter heterogeneities were incorporated in the proposed model with different MPs, including rate-dependent parameters. After the developed head model was verified, it was subjected to frontal, lateral, and posterior impact loadings, and the risks of TBI were investigated.

2. Materials and Methods

2.1. Head Model Geometry

Magnetic resonance (MR) scans, including 870 images with 250 µm thick slices, were obtained from the online database provided by Lüsebrink et al. [43] and were used to generate the geometry of the head model. Using 3D Slicer 5.0.1 software, the skull bone was identified by the provided segmentation tools and created as a single component. Then, the brain tissue was also identified from the image stacks, shown in Figure 1a, along the skull bone. The white and gray matter were also detected separately by appropriate thresholding (Figure 1a). The space between the skull and brain tissue were regarded as the cerebrospinal fluid (CSF) (Figure 1a). In addition, the facial bones were included in the model as a rigid part (Figure 1b), and the scalp was assumed as a nonstructural mass over the superior and posterior surfaces of the skull. Considering the vital functions of the midbrain and the prevalence of respective injuries in TBI investigations [3,4,44], it was regarded as an anatomical landmark (Figure 1a) to evaluate probable injury onset.

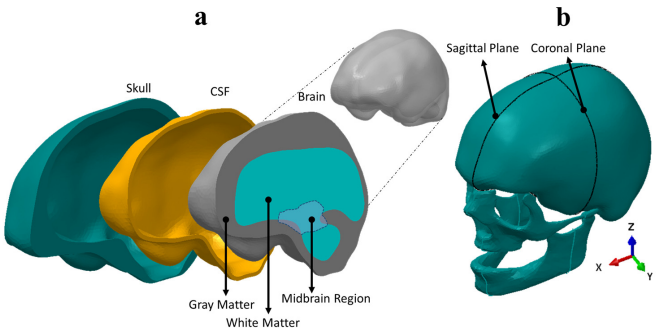


Figure 1. (**a**) An illustration of the major parts of the developed head model and the approximate anatomical location of the midbrain. (**b**) The geometry of the whole model, including the facial bones and mandible. The origin of the coordinate system is positioned at the midpoint of the line between the auditory meatus in the midsagittal plane. The Y-axis coincides with this line, with its positive direction from right to left. The Z-axis is in the midsagittal plane and is positive along the superior direction. Hence, the X-axis is positive anteriorly. It is represented outside the origin and next to the head model to visualize the directions better. The sagittal and coronal planes coincide with the X–Z and Y–Z planes, respectively.

Scalp and facial bone masses influence the physical properties of the head model, such as the total mass, center of gravity (COG), and moments of inertia. These mass values were determined based on previous studies, and are consistent with those reported in the literature [25]. The total mass, the center of gravity (COG), and the moments of inertia of the presented head model were calculated, and are shown next to the experimental evidence from Yoganandan et al. [45] in Table 1.

Table 1. Physical features of the head model and experimental measurements presented by Yoganandan et al. [45], based on the coordinate system of Figure 1.

	Mass (kg)	COG Coordinates (cm)			I_{XX} (kg.cm^2)	I_{YY} (kg.cm^2)	I_{ZZ} (kg.cm^2)
		X	Y	Z			
Head Model	3.92	1.4	−0.2	3.4	159	230	129
Experimental Measurement [45]	3.88 ± 0.47	1.3 ± 0.28	−0.1 ± 0.13	2.5 ± 1.08	174.9 ± 45.2	219.3 ± 50.8	159 ± 25.7

A right-hand coordinate system was used for physical measurements of the head model, similar to the study by Yoganandan et al. [45] (Figure 1). Through this validation step, the close association of the present model data with the experimental evaluations indicates the potential of the proposed model for TBI investigations.

2.2. Model MPs

Due to the importance of brain tissue mechanics in studying dynamic responses of the brain in the present head model, the CSF and skull were assumed to behave as linear elastic materials (Table 2). Although these assumptions may have affected the results, they favored a reduction in the computational complexity to help increase focus on the brain tissue. The choice of elastic properties for the CSF is common in similar previous studies [20,27,35], and it has been characterized as a very soft and incompressible material here (Table 2). Practically, the elastic behavior of the CSF was determined based on the assumption of incompressibility, with a bulk modulus of 2.16 GPa and a Poisson's ratio of 0.4999 [18]. Also, the density of the brain tissue was considered to be 1040 kg/m^3 [20,33].

Table 2. The physical and mechanical properties of the skull and CSF in the head model.

Model Components	Elastic Modulus (MPa)	Poisson's Ratio	Density (kg/m^3)	References
Skull	10,000	0.21	1800	[46,47]
CSF	1.314	0.4999	1040	[20]

Due to its very soft nature and its high water content, brain tissue has shown hyperelastic, time-dependent, and incompressible behaviors [11–13,48]. In order to investigate the effects of the brain tissue MPs on the head model behavior, three different constitutive models were allocated from previous studies on the brain tissue.

In "Model I", the mechanical behavior of the brain tissue was assumed to be nonlinear elastic with material coefficients, based on Mihai et al. [48]. In this model, the same MPs were assigned for the white and gray matter. Also, the allocated material parameters of Model I were not extracted at impact loading rates.

Therefore, for Model II the nonlinear elastic properties of the white and gray matter were taken into account based on the experimental data of Jin et al. [11]. The mentioned data were collected at a strain rate of 30/s, which resembles head impact loading rates [44]. Model III incorporates the hyperelastic behavior in Model II, and also includes time-dependent characteristics of the white and gray matter. In the latter case, the material

parameters of the hyper-viscoelastic constitutive model were obtained by interpolating the data from the stress relaxation experiments of Finan et al. [12]. Indeed, a hyper-viscoelastic constitutive model was considered for Model III, with the instantaneous response of Model II. It is worth mentioning that all of the chosen data sets (for Models II and III) were gathered from experimental studies of human brain samples [11,12]. However, one limitation of the present study was the use of data collected from different individuals' brain tissue. Data were either from post-mortem experiments [11] or from brain samples obtained during epilepsy surgery [12]. For ethical reasons, such limitations exist in testing human brain tissue and affect the data. However, in the study by Finan et al. [12], an attempt was made to use healthy, non-epileptic samples that were collected as surgical waste from surgery procedures.

A general expression for the equation of motion can be represented through momentum balance, as follows:

$$\rho \frac{\partial^2 v}{\partial t^2} = \text{div } \sigma + \rho b \tag{1}$$

where ρ is the mass density, v is the displacement vector, σ is the stress tensor, so the divergence of this tensor would account for the internal force per unit volume, and b represents body forces per unit volume.

It is noteworthy that Equations (2)–(7) are presented below for further explanations regarding the process of determining coefficients of the constitutive models based on experimental data sets. The Ogden strain energy density function (SEDF) has been popular in brain tissue constitutive modeling [10,14,48] and head impact simulations [5,33]. The Ogden SEDF is expressed as a function of principal stretches (λ_1, λ_2, and λ_3), as follows:

$$U = \sum_{i=1}^{N} \frac{2\mu_i}{{\alpha_i}^2} ({\lambda_1}^{\alpha_i} + {\lambda_2}^{\alpha_i} + {\lambda_3}^{\alpha_i} - 3) \tag{2}$$

where N denotes the order of the Ogden SEDF, and μ_i and α_i are the material parameters. In the present study, N was chosen to be 4. Using the Ogden SEDF, in theory, the three principal values of the Cauchy stresses can be computed as follows:

$$\sigma_j = -p + \lambda_j \frac{\partial U}{\partial \lambda_j} = -p + \sum_{i=1}^{N} \frac{2\mu_i}{\alpha_i} ({\lambda_j}^{\alpha_i}) \;\; ; \;\; j = 1.\, 2.\, 3 \tag{3}$$

where p is an unknown scalar in this theoretical representation that must be determined from the equilibrium equations and the boundary conditions.

Under uniaxial tensile test conditions, with the stretch ratio given as λ_1, and considering the assumption of incompressibility of the brain tissue [10] ($\lambda_1\lambda_2\lambda_3 = 1$) and equal stretch ratios in the transverse directions ($\lambda_2 = \lambda_3 = {\lambda_1}^{-\frac{1}{2}}$), the Ogden SEDF is simplified as follows:

$$U = \sum_{i=1}^{N} \frac{2\mu_i}{{\alpha_i}^2} \left({\lambda_1}^{\alpha_i} + 2{\lambda_1}^{-\frac{\alpha_i}{2}} - 3 \right) \tag{4}$$

The associated principal Cauchy stress along the uniaxial testing direction (σ_1) is obtained according to the boundary conditions of the uniaxial tensile test ($\sigma_2 = \sigma_3 = 0$), as follows:

$$\sigma_1 = \sum_{i=1}^{N} \frac{2\mu_i}{\alpha_i} \left({\lambda_1}^{\alpha_i} - {\lambda_1}^{-\frac{\alpha_i}{2}} \right) \tag{5}$$

Furthermore, the principal nominal stress along the uniaxial testing direction (P_1) is calculated as follows:

$$P_1 = \sum_{i=1}^{N} \frac{2\mu_i}{\alpha_i} \left(\lambda^{\alpha_i - 1} - \lambda^{-\frac{\alpha_i}{2} - 1} \right) \tag{6}$$

Also, the shear time-dependent behavior of the brain tissue was represented by the Prony series of the generalized Maxwell model for the relative shear modulus:

$$g(t) = \frac{G(t)}{G_0} = \left(1 - \sum_{i=1}^{M} g_i \left(1 - e^{\frac{-t}{\tau_i}}\right)\right) \tag{7}$$

where $G(t)$ is the shear relaxation modulus, G_0 is the initial shear modulus, M indicates the number of branches with viscous terms, g_i is the relaxation coefficient, τ_i represents the relaxation times, which, for the generalized Maxwell, are the parameters for each branch, and t denotes time. In this study, M was set to 3, which was appropriate to capture the observed brain tissue's relaxation behavior in the obtained experimental data (Figure 2b,c).

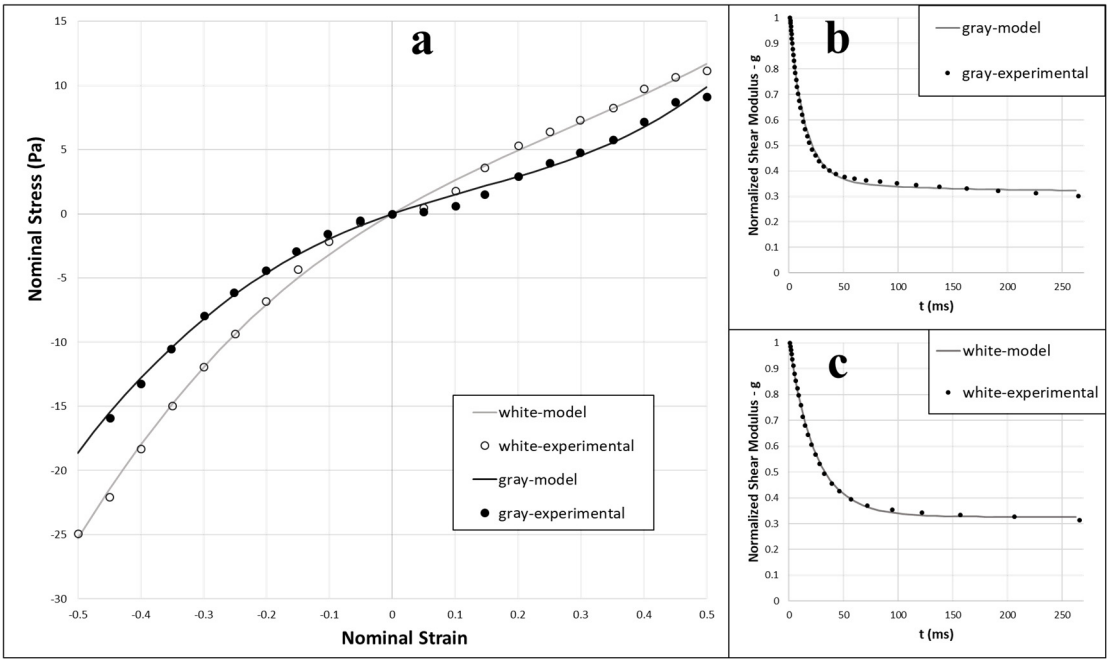


Figure 2. (**a**) Uniaxial extension–compression data for the gray and white matter (from [11]) and their respective fits with the Ogden hyperelastic SEDF. (**b**,**c**) Normalized relaxation data (from [12]) and the interpolated viscoelastic response for the gray and white matter, respectively.

The parameter μ represents the shear behavior in the Ogden SEDF. Therefore, in the resulting hyper-viscoelastic constitutive model based on it (Model III), μ is considered the time-dependent shear modulus, upon which the relaxation behavior is defined through the Prony series, as follows:

$$\mu(t) = \mu_0 \left(1 - \sum_{i=1}^{M} g_i \left(1 - e^{\frac{-t}{\tau_i}}\right)\right) \tag{8}$$

where $\mu(t)$ is the above-mentioned material parameter at each moment, and μ_0 is its initial or instantaneous value.

In order to allocate the material constants of the brain tissue from experimental data, curve fitting was carried out using a nonlinear optimization algorithm in MATLAB 2022 software. An objective function (x) was proposed as the difference between the model and empirical data, and the material parameters were allocated to minimize the objective function (interested readers can find more detail on the soft tissue constitutive modeling optimization procedure in [49]). In general, the optimization algorithm for determining

the material parameters of the constitutive model required minimizing the objective error function, according to the following equation:

$$x = \sum_{i=1}^{n} (C_m - C_e)^2 \quad (9)$$

where n represents the number of experimental data, C_e represents the experimental data, and C_m represents the parameters corresponding to the material models. In the case of the Ogden SEDF, the C parameter represents the nominal stress, and in the viscoelastic equation, it represents the relative shear modulus.

The experimental stress data for the white and gray matter [11] were fitted with the Ogden hyperelastic constitutive model (Figure 2a), and respective material parameters were determined (Table 3). Also, the fitted normalized relaxation of the generalized Maxwell model (Equation (7)) to the experimental data of Finan et al. [12] is represented in Figure 2 (panes b and c), respectively, for the gray and white matter. The allocated material parameters for the proposed three brain tissue models are reported in Table 3.

Table 3. MPs of the brain tissue in three constitutive models.

Model Type	Brain Component	Ogden Material Parameters								Viscoelastic Parameters in Prony Series					
		μ_1 (Pa)	α_1 (-)	μ_2 (Pa)	α_2 (-)	μ_3 (Pa)	α_3 (-)	μ_4 (Pa)	α_4 (-)	g_1 (-)	τ_1 (ms)	g_2 (-)	τ_2 (ms)	g_3 (-)	τ_3 (ms)
Model I (hyperelastic)	Gray matter White matter	−5877	2	5043	−2	2322	4	−1002	−4	-	-	-	-	-	-
Model II	Gray matter	45,670	1	−55,270	3	22,150	5	−6976	−2	-	-	-	-	-	-
(hyperelastic)	White matter	22,860	1	−15,790	3	7356	5	−4928	−2	-	-	-	-	-	-
Model III	Gray matter	45,670	1	−55,270	3	22,150	5	−6976	−2	0.1091	10	0.5237	15	0.0474	100
(hyper-viscoelastic)	White matter	22,860	1	−15,790	3	7356	5	−4928	−2	0.0578	15	0.6116	25	0.0082	250

2.3. Interface and Boundary Conditions

For all model components, continuity conditions were imposed at their interfaces, which is a common approach in similar studies [29,35,47]. This means that a common surface was defined between each pair of components in contact, causing no relative movement between them. As a result, it is implied that the mechanical parameters at these boundaries are consistent and shared among the contacting components. Although similar studies have employed the continuity conditions mentioned above, this option differs from realistic conditions with the possibility of relative movements. Therefore, such simplification represents a limitation of the present study, and future investigations can benefit from incorporating more complex definitions in this regard.

Furthermore, the facial bones and mandible area were tied to the skull. The effects of the neck joints on head dynamics were almost insignificant for the impact loading conditions [24]; hence, a free boundary condition without any constraint was acquired for this area in the present study.

2.4. Loading Conditions

The applied loading profile is shown in Figure 3a. The proposed loading regime was based on experiments by Nahum et al. [50]. In that experimental study, a seated human cadaver was hit on the head, specifically with impacts directed at the frontal bone along the midsagittal plane. Then, the intracranial pressure was measured at different spots over time, including a site behind the frontal bone near the impact area. The pressure in this spot was called the coup pressure. The coup pressure data from the experiments by Nahum et al. [50] are utilized to validate the present head model performance in the next section.

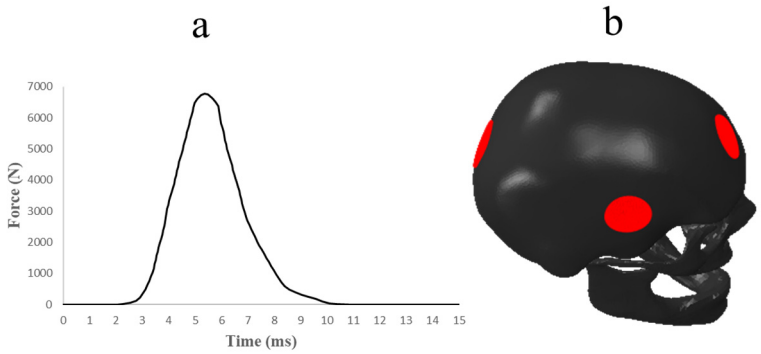


Figure 3. (**a**) The impact loading profile based on the Nahum et al. [50]. (**b**) The locations of different areas on the head subjected to impact loading.

The location of the impact is a determining factor in the biomechanics of the head. Hence, three mentioned loading profiles were applied on three sides of the head, namely the frontal, lateral (near the temporal area), and posterior (near the occipital bone) sides of the head (Figure 3b).

Mechanical analysis of the head model was carried out using ABAQUS 2017 software and the explicit dynamic method. The explicit solver is suitable for the simulation of dynamic cases, like high-speed head impacts, because it can better handle high strain rates, nonlinearities, rapidly changing stress and strain states, and large deformations or material damages; this is because it does not require an implicit tangent stiffness matrix and it does not involve checking iterations or convergence criteria [31].

However, a limitation of an explicit method is its inability to strictly enforce incompressibility, unlike implicit approaches that may solve for pressure as a separate field variable. Explicit methods approximate near-incompressible properties through constitutive responses of the material, which may influence predictions of the pressure response. Despite this limitation, explicit approaches have been commonly used for studying head impact dynamics [5,20,29,31,34,35,37], providing computational efficiencies and the possibility of investigating the mechanics of head components like brain tissue.

Mesh-convergence was attained with 106,372 quadratic tetrahedral elements. In this process, to investigate whether the results were independent of the mesh used, the impact on the head model was performed in cases of different numbers of elements. By gradually increasing the number of elements, the maximum internal energy values of the head model were analyzed. Then, the desired number of elements was selected when the differences decreased and reached an almost stable state where variations were less than 0.5%.

To verify the performance of the head model, after the frontal loading, coup pressure was gathered from beneath the impact site in the CSF region and compared with the results of Nahum et al. [50]. The values obtained for the constitutive Model I were utilized in the verification step. In the next step, responses from Models I, II, and III were investigated under the same frontal loading. Then, the effects of loading location (the frontal, posterior, and lateral sides of the head) were studied on Model III, incorporating the viscous effects.

As mentioned in the study by Chen and Ostoja-Starzewski [29] regarding the decoupling of dilatation (pressure) and distortion (shear) or deviatoric parts in the equation of motion of a homogeneous material, the mechanical response of the brain can be separated into dilatational (related to volume changes) and deviatoric (related to shape changing without volume alteration) behaviors. Pressure, as an important dilatational variable [42], and von Mises stresses, as the representative deviatoric behavior [29], were studied for the proposed head model. Pressure is defined as the mean value of the three principal stresses,

while the von Mises stress, as a measure of deviatoric response, is based on the differences between the principal stresses. These two mechanical measures are represented as follows:

$$Pressure = \frac{\sigma_1 + \sigma_2 + \sigma_3}{3} \tag{10}$$

$$\sigma_{von\ Mises} = \sqrt{\frac{1}{2}\left((\sigma_1 - \sigma_2)^2 + (\sigma_2 - \sigma_3)^2 + (\sigma_1 - \sigma_3)^2\right)} \tag{11}$$

where $\sigma_{von\ Mises}$ is the von Mises stress, and σ_1, σ_2, and σ_3 denote the principal stresses.

For a more comprehensive investigation of deviatoric responses at different loading locations, the stress values were compared along specific pathlines for the three loading cases. These pathlines started near the impact site, spanning the head COG (near the corpus callosum), and reached the opposite side of the brain (Figure 4). Each pathline included a set of 30 elements with approximately 4 mm steps selected, and stress values were extracted. In each case, the first element in the impact site was numbered 1, and the last element on the opposite side was numbered 30.

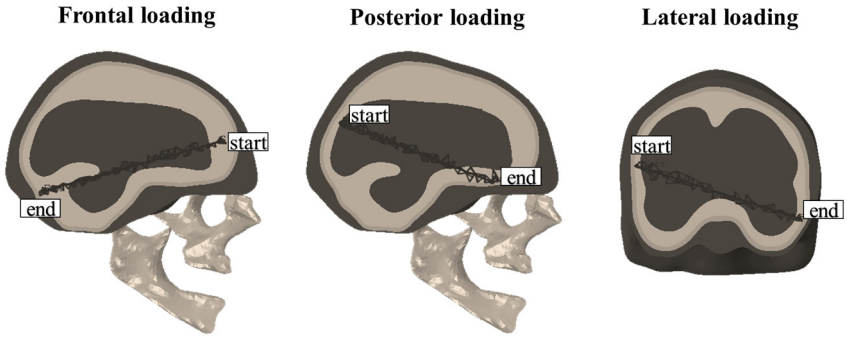


Figure 4. Data extraction pathlines, including the start and end points for each of the frontal and posterior loadings (sagittal view) and the lateral loading (coronal view).

3. Results and Discussion

3.1. Model Verification

The coup pressure profile of the head model (Model I) was compared against the experimental results of Nahum et al. [50], as shown in Figure 5. Using this experimental data for the performance validation of different head models is also common in other studies [5,20,24]. The agreement between the model and the experimental data was assessed using metrics such as the difference in peak pressure magnitude, being a low value of about 23 kPa. Also, a difference of less than 0.5 milliseconds was observed regarding the timing of the peak pressure value.

Although the maximum pressure value of the model is about 13% higher than the respective experimental pressure, the general agreement between the simulation and experiment outcomes indicates the validity of the proposed head model for further head impact studies.

Using the mentioned impact data to investigate the performance of head models by comparing it with experimental conditions is common in similar studies [3,5,20,21,29,47,51]. However, the limitations caused in this regard include the fact that the Nahum et al. [50] study was not recent and was conducted on cadavers.

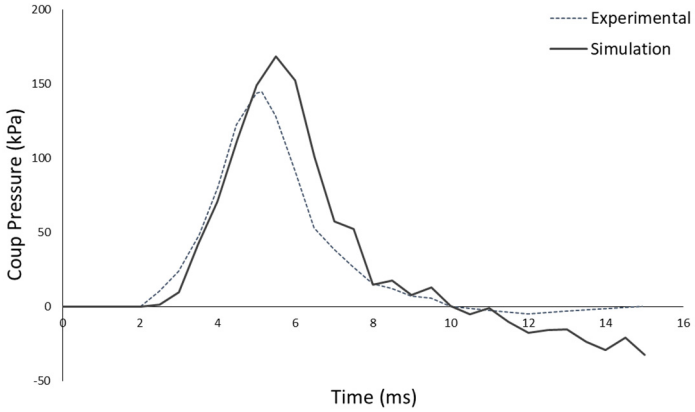


Figure 5. The coup pressure trend for the proposed head model (using Model I) and the cadaver experiments by Nahum et al. [50]. For both cases, the same frontal regions of the skull were loaded with the impact loading profile shown in Figure 3a.

3.2. Significance of Brain MPs

In Figure 6, the distributions of brain pressure for the three proposed models are presented on the sagittal plane at time steps of 3, 5, 7, 9, and 11 ms. For the three models with different brain MPs, no apparent differences in respective pressure distribution were noticeable (Figure 6). Such similar pressure contours for the three models are most likely due to the incompressibility constraint of the brain tissue. The high bulk modulus provided a nearly incompressible state for the brain tissue. Such behavior was associated with considerably high dilatational wave speeds [29]. Hence, even for short time intervals in the order of milliseconds, as seen in impact loading, the dilatational pressure waves would have many reflections in the bounded environment of the skull. As a result, at any instant of loading time, a dynamic equilibrium state is depicted, mostly independent of the brain MPs (Figure 6). Noticeable negative pressure at the opposite side of the impact in the 4–7 ms period might also have injured the respective regions [52].

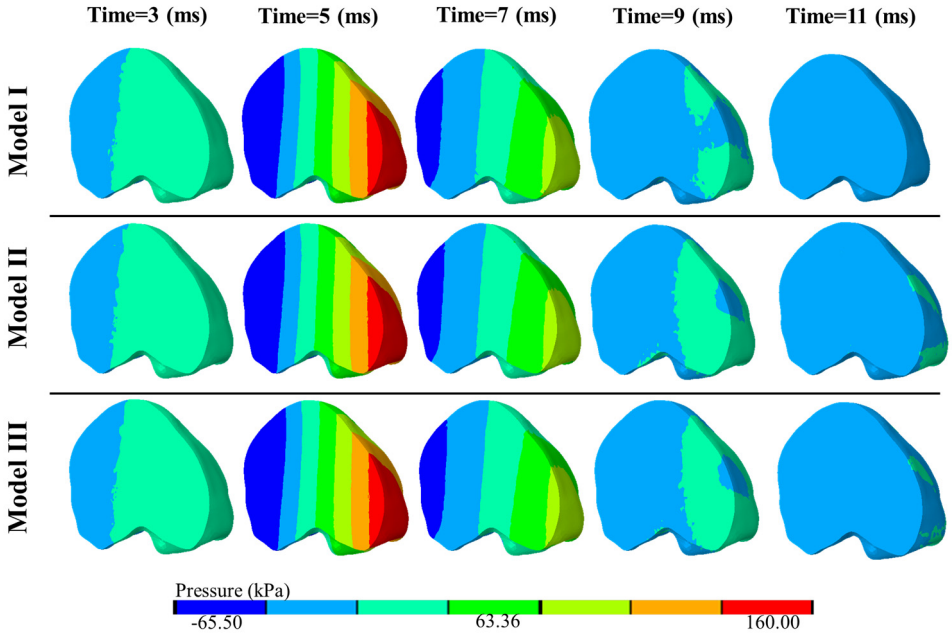


Figure 6. Brain pressure regimes for the three models of the brain at different time steps during the impact loading. For the range of proposed constitutive models, the maximum pressure values are observed at 5 ms, which coincides with the time of peak impact load.

Based on the von Mises stress contours of the brain at different time steps in Figure 7, shear waves moved from the surface of the gray matter toward the inner white matter region. Despite the respective dilatational behaviors, the brain's deviatoric responses mainly depended on the proposed constitutive models.

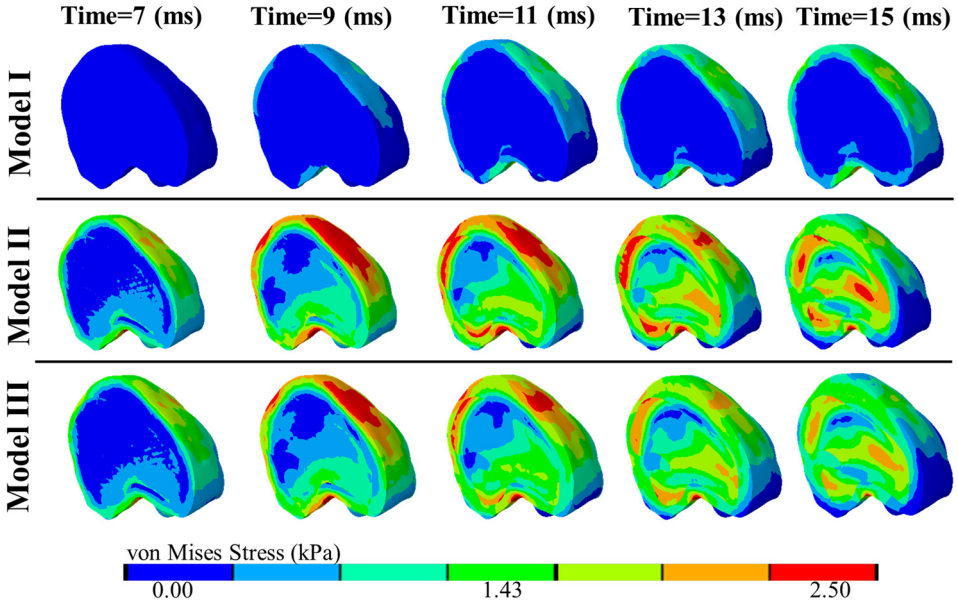


Figure 7. Von Mises stress contours of the brain models during the 15 ms interval. The impact loading diminishes after 10 ms, but the shear waves still exist after 15 ms. Markedly lower stress values for Model I are evident. The viscoelastic behavior of the gray and white matter in Model III proposes lower von Mises stresses than the respective hyperelastic model (Model II).

The observed differences between the deviatoric and dilatational behaviors arise from the lower speed of the shear waves compared to the dilatational waves [29]. Such lower wave speed made it possible to observe the differences between the performances of the constitutive models (especially Model I) in short periods of impact loadings. Notably, propagated shear waves did not diminish even after unloading at 10 ms, and von Mises stresses keep fluctuating in the brain (t = 13 ms and t = 15 ms in Figure 7).

In the case of Model I, the von Mises stress values were significantly lower compared to the respective time steps of the other two models (Figure 7). Noticeably, lower stress values for the inner brain regions in Model I were observed because the respective constitutive model is not based on impact experiments, and hence underestimates the brain tissue stresses in impact loading.

Although the overall patterns of deviatoric behavior were similar for the respective time steps of Models II and III, lower von Mises stresses were observed in the case of Model III, especially for the last 4 milliseconds (Figure 7). The viscous damping characteristics of Model III led to the observed lower stress values compared to Model II. The brain tissue and its main components were proven to demonstrate nonlinear elastic and time-dependent responses [12,13], and viscous effects were part of their nature.

It could be concluded that Model III (hyper-viscoelastic) is the most suitable here for studying head impacts and investigating TBI incidence. However, this is based on the specific experimental data that indicates material parameters. It is acknowledged that this finding may have limitations in its application for broad accident scenarios. Therefore, further investigation is encouraged under varying conditions as well.

The maximum shear stress of the midbrain area (as a valid used injury criterion) in Models II and III was 2.44 kPa and 2.13 kPa, respectively, while in Model I, such stress

(0.64 kPa) was less than the other two cases. According to the criteria of TBI occurrence [3], in Models II and III, the brain tissue was more near to the borderline of damage incidence.

It was shown that brain pressures did not provide enough detail on the time steps of the impact (in the order of milliseconds), and they rapidly reached an equilibrium state, while the shear waves existed in the head even after the impact. Therefore, deformations and deviatoric behaviors were crucial for these studies.

Although care was taken to select appropriate experimental data and indicate models for the brain tissue so that the present model could have good performance in general investigations of head impacts, there are still differences between individuals regarding the properties of their brain tissue, which may cause differences between studies using a single head model. Such differences are among the limitations of using a patient-specific head model, which affect their practicality aspect, besides their applicability.

3.3. Effect of Loading Location

Figure 8 depicts the von Mises stress contours of shear wave propagation during the impact loading in different locations. Stress values for the lateral loading were significantly higher than the other two loading cases. To perform a neat comparison of the cases, maximum values of brain pressures, von Mises stresses, and nominal strains in the midbrain area for all impact cases were collected, as shown in Table 4. The differences between the lateral loading and the other two cases are remarkable. The maximum pressure in the lateral loading case is more than twice that of the other cases, and the maximum von Mises stresses and nominal strains are more than three times their respective parameters in the frontal and posterior impact cases.

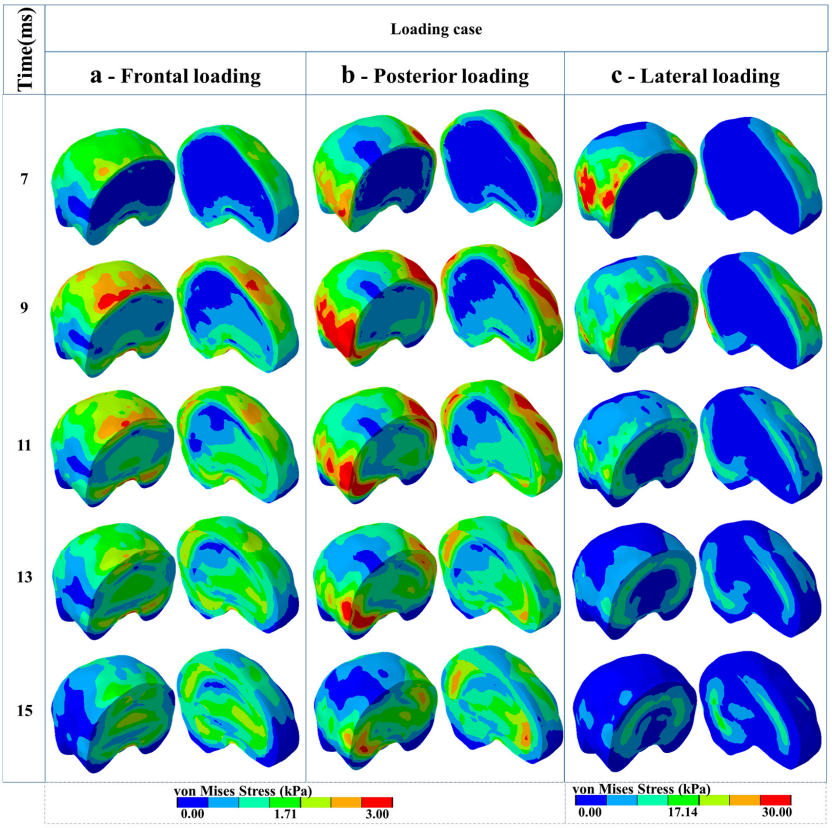


Figure 8. Von Mises stresses distribution for impact loading on frontal, posterior, and lateral locations on the head. The contours of the lateral loading have a different scale because of one-order-higher stress values.

Table 4. The maximum values of brain pressure, von Mises stress, and nominal strain in the midbrain area for impact loading on three different head locations.

Load Case	Frontal	Posterior	Lateral
Maximum brain pressure (kPa)	159.4	178.8	467.9
Maximum von Mises stress of midbrain (kPa)	1.9	2.2	7.7
Maximum nominal strain of midbrain	0.078	0.089	0.284

Based on the previous literature, a brain pressure of 173 kPa poses a minimal risk of damage, while pressures exceeding 200 kPa are associated with high risks of contusions, edema, and hematoma [4]. According to the values given in Table 4, the maximum pressure for the posterior impact case is within the injury threshold, and the lateral loading case demonstrates severe TBI incidence. Strains beyond 0.26 in the midbrain are reported to increase the incidence of mild traumatic brain injury or concussion by 25% [4]. However, the maximum strain values in the frontal and posterior loadings do not pose such risks of brain injury, though the strain for the lateral loading case is beyond the given threshold.

To observe the trend of stress changes more closely, the pathlines defined earlier were focused on (Figure 4). Accordingly, von Mises stress curves are reported for the second half of the loading interval, which is associated with peak values of the stress wave in the brain (Figure 8). These curves can represent the considerable effects of shear waves on the internal areas of the brain. For the frontal loading, stresses over the entire pathline increase in the first two time steps of 7 and 9 ms. Following the effect of deviatoric waves, the maximum stress values do not reduce noticeably at subsequent time steps (Time = 11 to 15 ms, Figure 9a). In the gray matter near the two endpoints, no considerable stress changes are evident after 11 ms (Figure 9a).

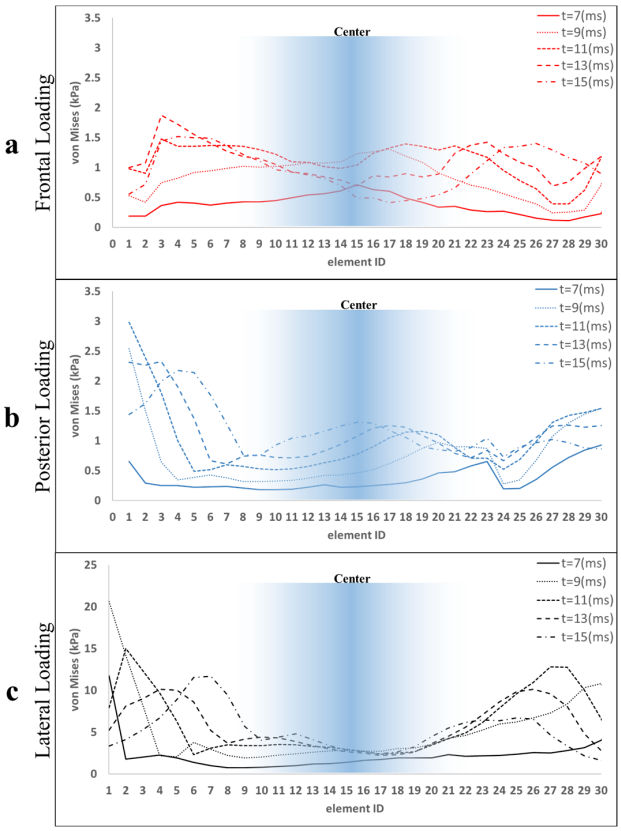


Figure 9. Changes in von Mises stress along the introduced pathlines for the head's frontal, posterior, and lateral loading. A different set of axis limits was adopted for the lateral loading, because of much higher von Mises stresses in this case.

For the posterior loading (Figure 9b), near the impact site, the stresses are significantly higher than in the center. In addition, shear waves are observable near the two endpoints of the pathline, especially for the 11–15 ms range. Consistently with the general trend (posterior loading in Figure 8b), a shift in local shear wave peaks toward the center and slightly reduced stress values are also noticeable.

The incidence of stress peaks near the corpus callosum indicates shear wave propagation into the white matter areas. In the frontal loading, the initially observed inner wave peak moves away from the center over time (Figure 9a, t = 11 to 15 ms). However, for the loading on the posterior side of the head, the peak is observed close to the end of the curve (far from the loading site), and it moves toward the center and reaches the corpus callosum area at the final time step (Figure 9b, t = 15 ms). In both the frontal and posterior loadings, the inner peak stresses relocate towards the back of the head. The peak magnitude increases slightly for the posterior loading case. However, the central areas demonstrate lower stresses compared to the endpoints, showing low shear wave propagations into these areas.

For the loading on the lateral side, stresses near both endpoints rapidly rise and show faster decay. For most of the inspected interval, shear waves remain out of the central areas of the brain. Only in the last 4 ms, after the relaxation of impact loading, do the waves advance toward the corpus callosum area (~pathline center), although the stress values in this area are minimal compared to the endpoints (Figure 9c). The shear waves propagate more rapidly in the lateral and posterior loadings. This is compatible with general observations of stress contours (Figure 8b,c) and highlights the importance of shear waves in the cortex areas and the gray matter, while propagations into the white matter areas are lower in these two loadings. On the other hand, compared to the other two loading scenarios, stress values near the corpus callosum are higher than the endpoints for the frontal loading (Figure 9a). Therefore, the corpus callosum and other internal components of the brain are more susceptible to damage accumulation and consequent adversities.

The observed distinctions for the studied impact locations arise from the asymmetric and complex geometry of the head and its compartments. Because of the higher stiffness of the skull compared to other components of the head, respective stress wave transmissions are much faster than those of the brain tissue. With the given complications of the head model, observed differences in stress patterns are due to these heterogeneities. However, these observations underline the importance of designing more sophisticated head protection devices, as the brain's resulting stress state depends on the location of impact loading.

The loading conditions used in the present study give a general idea of head impacts, but they are based on simpler scenarios, and might not fully represent the complexity of real-world incidents. Vast variability in factors like the loading angle, force, and duration of the impact, or variations in individual body structures, could lead to more complex conditions.

4. Conclusions

This study focused on allocating appropriate constitutive models of the brain tissue for impact loading conditions. A patient-specific finite element head model was developed for this purpose. The von Mises stresses, as a deviatoric response, denoted marked differences between the brain constitutive models. Model I was unsuitable for reflecting the brain response under impact loading, since it was not based on impact experiments, and its respective stiffness was lower than the other models. The hyper-viscoelastic Model III provided a reasonably accurate framework for studying brain deviatoric responses and investigating TBI occurrence. In addition, among the impact loadings on the head's frontal, lateral, and posterior regions, lateral loading indicated a significantly higher risk of TBI

incidence, with much higher stress values. The impact consequences are not confined to the impact time, and stress fluctuations after the relaxation of the impact load might also lead to TBI. The reported head impact results and critical regions can help in the development of protective features such as helmets and airbags.

Author Contributions: Conceptualization, H.T. and I.Z.O.; methodology, A.G., H.T. and I.Z.O.; software, A.G.; validation, A.G., H.T. and I.Z.O.; formal analysis, A.G., H.T. and I.Z.O.; investigation, A.G. ; resources, H.T. and I.Z.O.; data curation, A.G.; writing—original draft preparation, A.G.; writing—review and editing, A.G., H.T., I.Z.O. and F.A.O.F.; visualization, A.G.; supervision, H.T. and I.Z.O.; project administration, H.T., I.Z.O. and F.A.O.F.; funding acquisition, F.A.O.F. All authors have read and agreed to the published version of the manuscript.

Funding: This article was supported by the projects UIDB/00481/2020 and UIDP/00481/2020—Fundação para a Ciência e a Tecnologia, DOI: 10.54499/UIDB/00481/2020 and DOI: 10.54499/UIDP/00481/2020.

Data Availability Statement: The original contributions presented in this study are included in the Article. Further inquiries can be directed to the corresponding authors.

Conflicts of Interest: The authors declare no conflicts of interest.

References

1. Nguyen, R.; Fiest, K.M.; McChesney, J.; Kwon, C.S.; Jette, N.; Frolkis, A.D.; Atta, C.; Mah, S.; Dhaliwal, H.; Reid, A.; et al. The international incidence of traumatic brain injury: A systematic review and meta-analysis. *Can. J. Neurol. Sci.* **2016**, *43*, 774–785. [CrossRef]
2. Taylor, C.A.; Bell, J.M.; Breiding, M.J.; Xu, L. Traumatic brain injury–Related emergency department visits, hospitalizations, and deaths—United States, 2007 and 2013. *MMWR Surveill. Summ.* **2017**, *66*, 1–16. [CrossRef]
3. Tse, K.M.; Lim, S.P.; Tan, V.B.C.; Lee, H.P. A Review of Head Injury and Finite Element Head Models. *Am. J. Eng. Technol. Soc.* **2015**, *1*, 28–52.
4. Fernandes, F.A.O.; Alves de Sousa, R.J.; Ptak, M. *Head Injury Simulation in Road Traffic Accidents*; Springer International Publishing: Berlin/Heidelberg, Germany, 2018.
5. Fernandes, F.A.; Tchepel, D.; de Sousa, R.J.A.; Ptak, M. Development and validation of a new finite element human head model: Yet another head model (YEAHM). *Eng. Comput.* **2018**, *35*, 477–496. [CrossRef]
6. Cinelli, I.; Destrade, M.; McHugh, P.; Trotta, A.; Gilchrist, M.; Duffy, M. Head-to-nerve analysis of electromechanical impairments of diffuse axonal injury. *Biomech. Model. Mechanobiol.* **2019**, *18*, 361–374. [CrossRef] [PubMed]
7. Miller, K.; Chinzei, K. Constitutive modelling of brain tissue: Experiment and theory. *J. Biomech.* **1997**, *30*, 1115–1121. [CrossRef] [PubMed]
8. Miller, K.; Chinzei, K. Mechanical properties of brain tissue in tension. *J. Biomech.* **2002**, *35*, 483–490. [CrossRef]
9. Coats, B.; Margulies, S.S. Material properties of porcine parietal cortex. *J. Biomech.* **2006**, *39*, 2521–2525. [CrossRef] [PubMed]
10. Franceschini, G.; Bigoni, D.; Regitnig, P.; Holzapfel, G. Brain tissue deforms similarly to filled elastomers and follows consolidation theory. *J. Mech. Phys. Solids* **2006**, *54*, 2592–2620. [CrossRef]
11. Jin, X.; Zhu, F.; Mao, H.; Shen, M.; Yang, K.H. A comprehensive experimental study on material properties of human brain tissue. *J. Biomech.* **2013**, *46*, 2795–2801. [CrossRef]
12. Finan, J.D.; Sundaresh, S.N.; Elkin, B.S.; McKhann, G.M.; Morrison, B. Regional mechanical properties of human brain tissue for computational models of traumatic brain injury. *Acta Biomater.* **2017**, *55*, 333–339. [CrossRef]
13. Budday, S.; Sommer, G.; Birkl, C.; Langkammer, C.; Haybaeck, J.; Kohnert, J.; Bauer, M.; Paulsen, F.; Steinmann, P.; Kuhl, E.; et al. Mechanical characterization of human brain tissue. *Acta Biomater.* **2017**, *48*, 319–340. [CrossRef] [PubMed]
14. Budday, S.; Sommer, G.; Haybaeck, J.; Steinmann, P.; Holzapfel, G.; Kuhl, E. Rheological characterization of human brain tissue. *Acta Biomater.* **2017**, *60*, 315–329. [CrossRef] [PubMed]
15. Murphy, M.C.; Huston, J.; Ehman, R.L. MR elastography of the brain and its application in neurological diseases. *NeuroImage* **2019**, *187*, 176–183. [CrossRef] [PubMed]
16. Arani, A.; Manduca, A.; Ehman, R.L.; Huston, J. Harnessing brain waves: A review of brain magnetic resonance elastography for clinicians and scientists entering the field. *Br. J. Radiol.* **2021**, *94*, 20200265. [CrossRef]
17. Ueno, K.; Melvin, J.W.; Li, L.; Lighthall, J.W. Development of Tissue Level Brain Injury Criteria by Finite Element Analysis. *J. Neurotrauma* **2009**, *12*, 695–706. [CrossRef]
18. Miller, K.; Chinzei, K.; Orssengo, G.; Bednarz, P. Mechanical properties of brain tissue in-vivo: Experiment and computer simulation. *J. Biomech.* **2000**, *33*, 1369–1376. [CrossRef]

19. Claessans, M.; Sauren, F.; Wismans, J. Modeling of the human head under impact conditions: A parametric study. In *Stapp Car Crash*; SAE International: Warrendale, PA, USA, 1997; pp. 315–328.
20. Tse, K.M.; Bin Tan, L.; Lee, S.J.; Lim, S.P.; Lee, H.P. Development and validation of two subject-specific finite element models of human head against three cadaveric experiments. *Int. J. Numer. Methods Biomed. Eng.* **2014**, *30*, 397–415. [CrossRef]
21. Yang, B.; Tse, K.-M.; Chen, N.; Tan, L.-B.; Zheng, Q.-Q.; Yang, H.-M.; Hu, M.; Pan, G.; Lee, H.-P. Development of a finite element head model for the study of impact head injury. *BioMed Res. Int.* **2014**, *2014*, 1–14. [CrossRef] [PubMed]
22. Garcia-Gonzalez, D.; Jayamohan, J.; Sotiropoulos, S.; Yoon, S.-H.; Cook, J.; Siviour, C.; Arias, A.; Jérusalem, A. On the mechanical behaviour of PEEK and HA cranial implants under impact loading. *J. Mech. Behav. Biomed. Mater.* **2017**, *69*, 342–354. [CrossRef]
23. Schroder, A.; Lawrence, T.; Voets, N.; Garcia-Gonzalez, D.; Jones, M.; Peña, J.M.; Jerusalem, A. A Machine Learning Enhanced Mechanistic Simulation Framework for Functional Deficit Prediction in TBI. *Front. Bioeng. Biotechnol.* **2021**, *9*, 587082. [CrossRef]
24. Ruan, J.S.; Khalil, T.; King, A.I. Dynamic response of the human head to impact by three-dimensional finite element analysis. *J. Biomech. Eng.* **1994**, *116*, 44–50. [CrossRef]
25. Zhou, C.; Khalil, T.B.; King, A.I. *A New Model Comparing Impact Responses of the Homogeneous and Inhomogeneous Human Brain*; SAE Transactions: Warrendale, PA, USA, 1995; pp. 121–137.
26. Garcia-Gonzalez, D.; Race, N.S.; Voets, N.L.; Jenkins, D.R.; Sotiropoulos, S.N.; Acosta, G.; Cruz-Haces, M.; Tang, J.; Shi, R.; Jérusalem, A. Cognition based bTBI mechanistic criteria; a tool for preventive and therapeutic innovations. *Sci. Rep.* **2018**, *8*, 1–14. [CrossRef]
27. Zhang, L.; Yang, K.H.; Dwarampudi, R.; Omori, K.; Li, T.; Chang, K.; Hardy, W.N.; Khalil, T.B.; King, A.I. Recent Advances in Brain Injury Research: A New Human Head Model Development and Validation. *SAE Tech. Pap.* **2001**. [CrossRef]
28. Tzschätzsch, H.; Kreft, B.; Schrank, F.; Bergs, J.; Braun, J.; Sack, I. In vivo time-harmonic ultrasound elastography of the human brain detects acute cerebral stiffness changes induced by intracranial pressure variations. *Sci. Rep.* **2018**, *8*, 17888. [CrossRef] [PubMed]
29. Chen, Y.; Ostoja-Starzewski, M. MRI-based finite element modeling of head trauma: Spherically focusing shear waves. *Acta Mech.* **2010**, *213*, 155–167. [CrossRef]
30. Gomez-Cruz, C.; la Torre, M.F.; Lachowski, D.; Prados-De-Haro, M.; Hernández, A.E.d.R.; Perea, G.; Muñoz-Barrutia, A.; Garcia-Gonzalez, D. Mechanical and Functional Responses in Astrocytes under Alternating Deformation Modes Using Magneto-Active Substrates. *Adv. Mater.* **2024**, *36*, 2312497. [CrossRef] [PubMed]
31. Deng, X.; Du, Z.; Feng, H.; Wang, S.; Luo, H.; Liu, Y. Investigation on the Modeling and Reconstruction of Head Injury Accident Using ABAQUS/Explicit. *Bioengineering* **2022**, *9*, 723. [CrossRef]
32. Abdi, H.; Sánchez-Molina, D.; García-Vilana, S.; Rahimi-Movaghar, V. Revealing the role of material properties in impact-related injuries: Investigating the influence of brain and skull density variations on head injury severity. *Heliyon* **2024**, *10*, e29427. [CrossRef] [PubMed]
33. Kleiven, S. Predictors for traumatic brain injuries evaluated through accident reconstructions. *Stapp Car Crash J.* **2007**, *51*, 81–114. [CrossRef]
34. Subramaniam, D.R.; Unnikrishnan, G.; Sundaramurthy, A.; Rubio, J.E.; Kote, V.B.; Reifman, J. Cerebral Vasculature Influences Blast-Induced Biomechanical Responses of Human Brain Tissue. *Front. Bioeng. Biotechnol.* **2021**, *9*, 744808. [CrossRef] [PubMed]
35. Li, X.; Zhou, Z.; Kleiven, S. An anatomically detailed and personalizable head injury model: Significance of brain and white matter tract morphological variability on strain. *Biomech. Model. Mechanobiol.* **2021**, *20*, 403–431. [CrossRef] [PubMed]
36. Franceschini, G. *The Mechanics of Human Brain Tissue*; The University of Trento: Trento, Italy, 2006.
37. Li, X.; Sandler, H.; Kleiven, S. The importance of nonlinear tissue modelling in finite element simulations of infant head impacts. *Biomech. Model. Mechanobiol.* **2017**, *16*, 823–840. [CrossRef] [PubMed]
38. Elkin, B.S.; Gabler, L.F.; Panzer, M.B.; Siegmund, G.P. Brain tissue strains vary with head impact location: A possible explanation for increased concussion risk in struck versus striking football players. *Clin. Biomech.* **2019**, *64*, 49–57. [CrossRef] [PubMed]
39. Giudice, J.S.; Park, G.; Kong, K.; Bailey, A.; Kent, R.; Panzer, M.B. Development of Open-Source Dummy and Impactor Models for the Assessment of American Football Helmet Finite Element Models. *Ann. Biomed. Eng.* **2018**, *47*, 464–474. [CrossRef] [PubMed]
40. Takhounts, E.G.; Ridella, S.A.; Hasija, V.; Tannous, R.E.; Campbell, J.Q.; Malone, D.; Danelson, K.; Stitzel, J.; Rowson, S.; Duma, S. Investigation of traumatic brain injuries using the next generation of simulated injury monitor (SIMon) finite element head model. *Stapp Car Crash J.* **2008**, *52*, 1–31. [CrossRef] [PubMed]
41. Takhounts, E.G.; Eppinger, R.H.; Campbell, J.Q.; Tannous, R.E.; Power, E.D.; Shook, L.S. *On the Development of the SIMon Finite Element Head Model*; SAE Tech Pap 2003-Octob; SAE: Warrendale, PA, USA, 2003. [CrossRef]
42. Ruan, J.S.; Khalil, T.B.; King, A.I. Finite element modeling of direct head impact. In Proceedings of the Stapp Car Crash Conference, Warrendale, PA, USA, 1 November 1993.
43. Lüsebrink, F.; Sciarra, A.; Mattern, H.; Yakupov, R.; Speck, O. T1-weighted in vivo human whole brain MRI dataset with an ultrahigh isotropic resolution of 250 µm. *Sci. Data* **2017**, *4*, 170062. [CrossRef] [PubMed]

44. Viano, D.C.; Casson, I.R.; Pellman, E.J.; Zhang, L.; King, A.I.; Yang, K.H. Concussion in professional football: Brain responses by finite element analysis: Part 9. *Neurosurgery* **2005**, *57*, 891–916. [CrossRef] [PubMed]
45. Yoganandan, N.; Pintar, F.A.; Zhang, J.; Baisden, J.L. Physical properties of the human head: Mass, center of gravity and moment of inertia. *J. Biomech.* **2009**, *42*, 1177–1192. [CrossRef] [PubMed]
46. Mao, H.; Gao, H.; Cao, L.; Genthikatti, V.V.; Yang, K.H. Development of high-quality hexahedral human brain meshes using feature-based multi-block approach. *Comput. Methods Biomech. Biomed. Eng.* **2013**, *16*, 271–279. [CrossRef]
47. Belingardi, G.; Chiandussi, G.; Gaviglio, I. Development and validation of a new finite element model of human head. In Proceedings of the 19th International Technical Conference of the Enhanced Safety of Vehicle (ESV), Washington, DC, USA, 6–9 June 2005.
48. Mihai, L.A.; Chin, L.; Janmey, P.A.; Goriely, A. A comparison of hyperelastic constitutive models applicable to brain and fat tissues. *J. R. Soc. Interface* **2015**, *12*, 20150486. [CrossRef] [PubMed]
49. Taghizadeh, H.; Tafazzoli-Shadpour, M.; Shadmehr, M.B.; Fatouraee, N. Evaluation of biaxial mechanical properties of aortic media based on the lamellar microstructure. *Materials* **2015**, *8*, 302–316. [CrossRef]
50. Nahum, A.M.; Smith, R.; Ward, C.C. Intracranial pressure dynamics during head impact. In Proceedings of the Stapp Car Crash Conference Proceedings, New Orleans, LO, USA, 19–21 October 1977.
51. Abdi, H.; Sanchez-Molina, D.; Garcia-Vilana, S.; Rahimi-Movaghar, V. Quantifying the effect of cerebral atrophy on head injury risk in elderly individuals: Insights from computational biomechanics and experimental analysis of bridging veins. *Injury* **2023**, *54*, 111125. [CrossRef] [PubMed]
52. Martin, G. Traumatic brain injury: The first 15 milliseconds. *Brain Inj.* **2016**, *30*, 1517–1524. [CrossRef] [PubMed]

Disclaimer/Publisher's Note: The statements, opinions and data contained in all publications are solely those of the individual author(s) and contributor(s) and not of MDPI and/or the editor(s). MDPI and/or the editor(s) disclaim responsibility for any injury to people or property resulting from any ideas, methods, instructions or products referred to in the content.